Available online at www.sciencedirect.com
SCIENCE DIRECT
Journal of Catalysis 230 (2005) 317–326
JOURNAL OF CATALYSIS
www.elsevier.com/locate/jcat

Effect of titanium substitution on the structure of $VSbO_4$ catalysts for propane ammoxidation

Guang Xiong [a], Vivian S. Sullivan [a], Peter C. Stair [a,*], Gerry W. Zajac [b], Steven S. Trail [b], James A. Kaduk [b], Joseph T. Golab [b], James F. Brazdil [b]

[a] *Center for Catalysis and Surface Science, Northwestern University, 2137 Sheridan Road, Evanston, IL 60208-3000, USA*
[b] *BP Chemicals, 150 Warrenville Road, Naperville, IL 60566, USA*

Received 27 July 2004; revised 22 November 2004; accepted 22 November 2004

Abstract

The effect of titanium substitution on vanadium antimony oxide propane ammoxidation catalysts was investigated by UV Raman spectroscopy and X-ray diffraction. UV Raman spectra exhibit bands in the region of 450–1000 cm^{-1}, which are associated with the rutile structure, a cation vacancy site, and V_2O_5. Calculations of the vibrational frequencies made with the use of CASTEP optimized slab models provide good agreement with experimental results. With titanium substitution, the rutile bands shift and broaden. Comparison of freshly prepared and ground samples shows that crystalline V_2O_5 forms upon grinding in air. Titanium stabilizes vanadium in the vanadium antimonate rutile structure and thus prevents the formation of crystalline V_2O_5. An in situ Raman characterization of titanium-containing vanadium antimony oxide catalysts was made in reducing and oxidizing atmospheres. The band associated with two-coordinate oxygen at cation vacancy sites disappears under reduction conditions, then returns after reoxidation in air. This indicates that this lattice oxygen moiety is key to ammonia activation. The titanium-substituted sample shows additional characteristics that indicate titanium improves the reduction and oxidation capability of the vanadium antimonate catalyst.

1. Introduction

Selective ammoxidation of propane into acrylonitrile is of practical significance, as acrylonitrile is widely used in the petrochemical industry. Currently acrylonitrile is produced by the propylene ammoxidation process developed by Sohio [1]. Considering the cost of feedstocks, direct conversion of propane into acrylonitrile is an attractive alternative process [2–4]. However, the activity and selectivity of propane ammoxidation are much lower than those of propylene ammoxidation, as the C–H bond strength of the alkane is higher than that of the corresponding alkene. Numerous studies have focused on vanadium–antimony mixed oxides as catalysts for propane ammoxidation [5–17]. Vanadium–antimony mixed oxides typically contain several phases. In addition to a $VSbO_4$ rutile phase, Sb_2O_4, V_2O_5, and amorphous V and Sb oxides can be formed, depending on the preparation method and the Sb/V ratio [4]. It is accepted that a cation-deficient rutile $VSbO_4$ and α-Sb_2O_4 are the crucial phases for an efficient catalyst [2,9]. Vanadium ions are the primary active sites for the dehydrogenation of propane, whereas excess antimony is necessary for ammoxidation of the reaction intermediate propylene to acrylonitrile [9,11,15,17].

It has been found that the substitution of other cations for vanadium can improve the selectivity of a catalyst for acrylonitrile [12,13,15,16,18]. For example, a catalytic test of Sb–V–Ti oxides showed much better catalytic properties compared with the Sb–V–O system [13,15]. Andersson pointed out that the substitution contributes to the dilution and isolation of the V-sites, which are selective for acrylonitrile [15]. On the other hand, a study of $VSbFeO_4$ [16] showed that iron helps to stabilize the surface composition,

* Corresponding author.
E-mail address: pstair@northwestern.edu (P.C. Stair).

0021-9517/$ – see front matter © 2004 Published by Elsevier Inc.
doi:10.1016/j.jcat.2004.11.046

thus limiting the formation of surface antimony oxide during reaction. It was suggested that this effect might lead to more active but less selective catalysts. These results show that the substitution may play several roles, with different effects on catalytic properties. Thus, it is of interest to obtain direct information about the structure of the catalysts at the molecular level before and after substitution, paying attention in particular to the effect of the Ti substitution on the structure in both reductive and oxidative atmospheres.

Raman spectroscopy can be a useful technique for the study of the structure of vanadium–antimony mixed oxides, since it provides molecular-scale information through vibrational modes. However, it is usually difficult to study deeply colored samples by conventional Raman spectroscopy because of strong absorption in the visible region. Most of the peak assignments in Raman spectra have been derived from monophasic metal oxides, such as V_2O_5, Sb_2O_4, WO_3, and MoO_3 [9,12–14,19–21]. Little information on the $VSbO_4$ rutile phase has been reported.

UV Raman spectroscopy is a useful technique for the study of deeply colored materials [22–25]. In this paper we report on studies of the structure of $VSbO_4$ and $VSbTiO_4$ catalysts under oxidative and reductive atmospheres by UV Raman spectroscopy. The results provide insights into the effect of titanium substitution on the stability of V–Sb mixed oxides and the impact on catalytic properties.

2. Experimental

2.1. Computational methodology

Vanadium antimonate has a rutile structure, for which the most stable surface is the 110 Miller plane. Both six- and five-coordinate cation sites are present on the surface. Starting with the crystal structure for a typical rutile material (TiO_2), a crystalline, 3-dimensional periodic "slab" of the 110 plane is created. Metal atom sites are variably occupied by vanadium or antimony and, for simplicity, are fixed at 50% occupancy. See Fig. 1.

Another $VSbO_4$ model slab is made from this initial atomistic model, which contains a 5-fold Sb cation vacancy in the middle of the surface (see Fig. 2).

2.1.1. CASTEP optimization

All of the models described were built and fully optimized with the use of the Cerius^2 suite of molecular modeling software [26]. To determine the optimized geometric structures and total energy, the Density Functional Theory plane-wave pseudopotential program CASTEP [27] is applied to the 3D models, and the bottom two atomic layers are kept at the bulk structural parameters (see Fig. 3 for the optimized structure). A medium basis consisting of ultrasoft potentials on Mo, O, and Sb and charge-corrected ultrasoft potentials on V ($30 \times 64 \times 80$ FFT grid) and the GGA-PW91 functional are selected. In addition, a kinetic energy cutoff of 300 eV and a k-point spacing of 0.1 Å^{-1} (1 k-point) are chosen. For completeness, the metal SCF option is on and the MPI MatSci V4.6 Parallel version of CASTEP is applied.

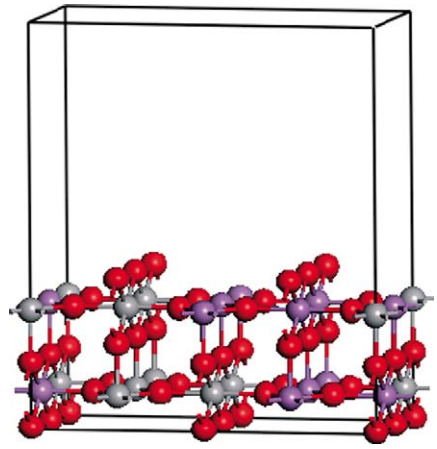

Fig. 1. $VSbO_4$ 110 "slab" consisting of 48 atoms; 32 O (red), 8 V (grey), and 8 Sb (purple). The overall dimensions of the slab are 6.1 Å × 13.1 Å × 15.8 Å with an additional 15 Å of vacuum over the surface.

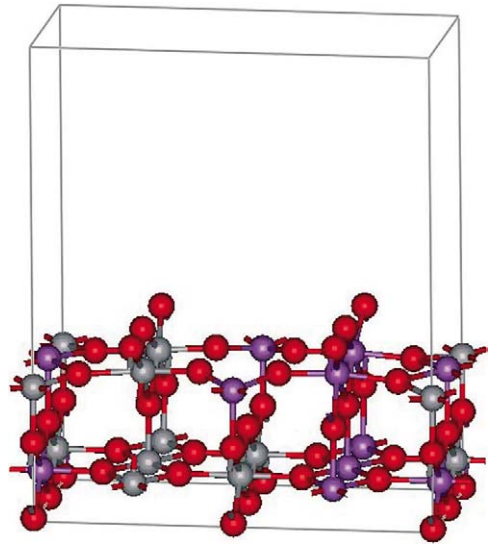

Fig. 2. VSb[ ]O_4 110 "slab" created from model in Fig. 1 consisting of 47 atoms; 32 O (red), 8 V (grey), and 7 Sb (purple). The missing antimony comes from a 5-fold site at the surface.

2.1.2. Infrared spectra

A comparison of the predicted IR spectra of these models with experimental results further aids our understanding of the surface structure. This paper provides access to a unique new method for probing the surface vibrational spectra of fluidized bed catalysts. Spectra of model $V_{8/9}Sb_{8/9}[\ ]_{2/9}O_4$ catalysts have attenuated bands at 460, 630, and 745 cm^{-1}. These bands are assigned to rutile-related bulk stretching modes. In addition, a strong band at 888 cm^{-1} is found (see Figs. 4 and 5).

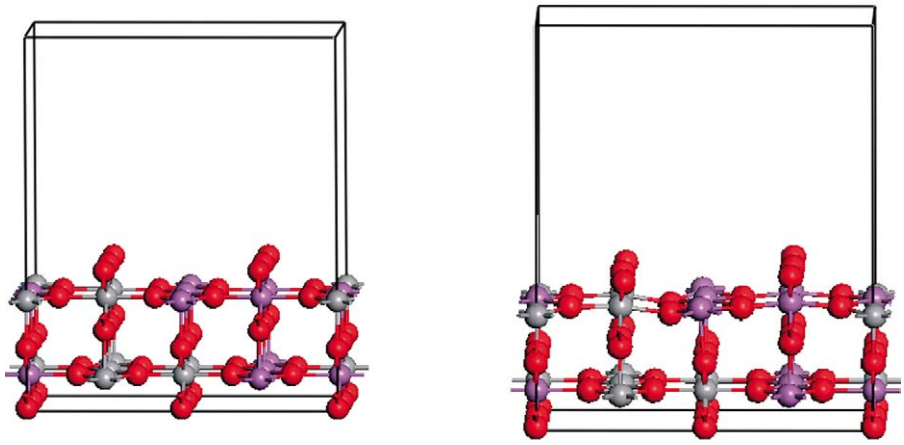

Fig. 3. The initial $VSbO_4$ 110 structure (left) is compared to the CASTEP optimized structure. O (red), V (grey), and Sb (purple).

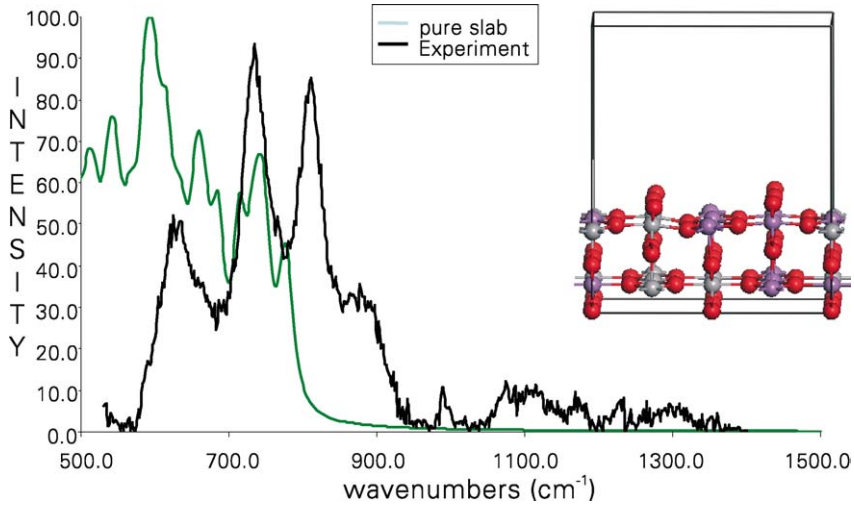

Fig. 4. The experimental spectrum for the $VSbO_x$ catalyst and the DMol3 predicted IR spectrum for the CASTEP optimized catalyst in which no Sb vacancy exists. The atom colors in all figures are: vanadium (grey), antimony (purple), and oxygen (red).

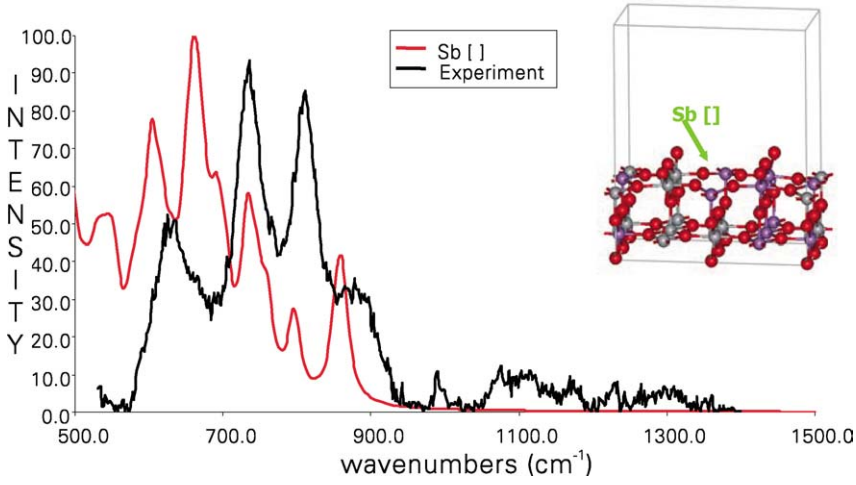

Fig. 5. The experimental spectrum for the $VSbO_x$ catalyst and the DMol3 predicted IR spectrum for the CASTEP optimized catalyst in which a 5-fold Sb vacancy exists. The atom colors in all figures are: vanadium (grey), antimony (purple), and oxygen (red).

2.1.3. DMol3-solid calculations

To better understand the origins of these peaks, we calculated IR spectra from the CASTEP-optimized slab structures with the use of the Density Functional Theory program [28] DMol3. (CASTEP cannot calculate IR spectra.) A single-point DMol3 energy and frequency calculation with the use of the PW91 functional and the DN basis is performed for the CASTEP-optimized slab. Because of computational time constraints, it is assumed that the optimized DMol3-solid structure would be very similar to the CASTEP-optimized structure. With this approximation, it is expected that DMol3 is capable of predicting the IR spectra with an accuracy of ±15–20% (100–300 cm^{-1} consistently). No transition dipole matrix elements were calculated to relate the calculated IR vibrational energies to the Raman intensities. However, we expect (when allowed) that the Raman vibrational bands are represented well by these calculated IR band positions.

More importantly, the vibrational mode motions of any predicted peak can be clearly identified from the output vibrational analysis of these calculations. Once the spectrum for the no-defect slab (Fig. 1) is determined, the vibrational mode of the attenuated bands at 460, 630, and 745 cm^{-1} is identified from the normal mode output. To compensate for the expected error in the spectrum predicted by DMol3 for the CASTEP-optimized structure, the *entire* calculational spectrum is shifted to produce the best alignment of these peaks with the experimental spectrum. No individual peaks are shifted; only a rigid band shift is applied to the calculated spectrum. These bands are chosen for alignment because they correspond to stretching modes of the bulk structure. Since the bottom two atomic layers of the models are kept at the bulk structural parameters, it is expected that their normal mode motions would correspond best to these experimental peaks. This fitting procedure leads to a rigid band red shift of 25 cm^{-1} for the predicted IR spectra. The fitted spectra have no "imaginary" frequencies.

2.2. Preparation

$V_{0.89}Sb_{0.89}[\ ]_{0.22}O_4$

$V_{0.76}Sb_{0.76}Ti_{0.30}[\ ]_{0.19}O_4$

$V_{0.62}Sb_{0.62}Ti_{0.60}[\ ]_{0.16}O_4$

Stratcor V_2O_5 (13.64 g) was added to a 660 ml of a 3 wt% H_2O_2 solution. The mixture was stirred until reaction of the vanadium pentoxide was complete, about 25 min. Laurel Sb_2O_3 powder (21.86 g) was added to the resulting red solution. This mixture was refluxed for 3 h to produce a black slurry. For the Ti samples 4.76 g or 7.77 g of Degussa P-25 TiO_2 powder was then added to the slurry. The mixture was then evaporated to dryness with constant stirring in a beaker on a hot plate. The material was further dried in air at 120 °C in a drying oven. The dried material was heat treated at 325 °C for 3 h, crushed to < 75 μm, then heated at 820 °C for 6 h, followed by postcalcination at 650 °C for 5 h. All heat treatments were conducted in air in a muffle furnace. The resulting solid was stirred in 100 ml of water for 1 h and then filtered. This was repeated 10 times. After the final treatment and filtering, the solid was dried at 120 °C. The Sb:V:Ti stoichiometry was confirmed by elemental analysis with the inductively coupled plasma technique.

We obtained ground samples by manually grinding the samples with a mortar and pestle for 2 min.

2.3. X-ray diffraction

X-ray powder diffraction patterns (5–100° 2θ, 0.02° steps, 12 s/step) were measured on a Rigaku D/MAX-B diffractometer equipped with a scintillation counter and a graphite diffracted beam monochromator. Quantitative phase analyses were carried out with the Rietveld method, with the use of GSAS [29]. Different refinement strategies were used for the $VSbO_4$- and the Ti-containing catalysts. For the base catalysts, the rutile structure was not refined. Scale factors and the lattice parameters were refined for all three phases. β-Sb_2O_4 exhibited a strongly preferred orientation (the result of platy morphology), and eighth-order spherical harmonic terms were refined. The profiles were described by the pseudo-Voigt function #2, but only the Lorentzian size broadening X profile coefficients and a common specimen displacement parameter were refined for each phase. For the Ti catalysts, the oxygen position and U_{iso} were refined subject to soft constraints of 1.98(1) Å on the M–O distances. The Ti occupancy of the metal site was fixed at the stoichiometric value, and the V/Sb occupancies were constrained to be equal; the total site occupancy was not constrained. A scale factor and the lattice parameters of the rutile phase were refined. The peak profiles were also described by pseudo-Voigt function #2; the Gaussian strain broadening coefficient U, the Lorentzian size broadening terms X and *ptec* (unique axis [001]), and *asym* were refined. The background in each pattern was described by a six-term cosine Fourier series.

2.4. UV Raman spectroscopy

Details of the UV Raman instrument and the fluidized bed reactor have been described elsewhere [22,23]. All Raman experiments were performed with 244-nm laser excitation with a power of about 15 mW. In a typical in situ Raman experiment, pellet samples were placed on the stainless-steel disk in the fluid bed reactor. The samples were heated to 480 °C in He, then NH_3 was introduced into the reactor for a few minutes. After reduction the samples were cooled to room temperature in He. The Raman spectra were recorded in He at room temperature. During reoxidation the samples were heated to 480 °C in He, and then the He gas was replaced with air. The samples were oxidized in air for several hours and then cooled in He. Finally, the Raman spectra were measured in He at room temperature.

3. Results

$VSbO_4$ and $VSbTiO_4$ catalysts were characterized by X-ray diffraction (XRD) and UV Raman spectroscopy. Fig. 6 shows X-ray powder diffraction patterns of the two ground catalysts. Table 1 shows the phase compositions and unit cell parameters for freshly prepared and ground samples determined by XRD. The bumpy surface of the unground $VSbO_4$ limited the accuracy of the quantification. Compared with the freshly prepared catalysts, the ground samples had a smaller average crystallite size. The fresh $VSbO_4$ catalyst contained three phases: the $VSbO_4$ rutile phase, crystalline V_2O_5, and β-Sb_2O_4. α-Sb_2O_4 had been observed in previous work [8,13,32]; the formation of β-Sb_2O_4 is attributed to calcination at higher temperature (820 vs 810 °C) and longer time (6 vs 1 h) in the preparation of the material reported here. The rutile $VSbO_4$ comprised ∼ 68% of the catalyst. A significant concentration of β-Sb_2O_4 (∼ 30%) was present, as was a trace of V_2O_5 (∼ 2%). After we ground the sample, the concentration of rutile $VSbO_4$ decreased by 13 wt%, whereas that of V_2O_5 increased by 12 wt%. The amount of β-Sb_2O_4 remained approximately constant, increasing by only 1 wt%. The titanium-substituted catalyst behaved differently. Both fresh and ground $VSbTiO_4$ consist of a single phase, rutile $V_{0.76}Sb_{0.76}[\,]_{0.19}Ti_{0.3}O_4$. No crystalline V_2O_5, β-Sb_2O_4, or TiO_2 was detectable in these samples. The lattice constants and cell volume of the Ti-substituted sample decreased after grinding; the volume decreased by 15 estimated standard deviations, but the absolute change was very small. No significant changes in lattice constants were observed after grinding. The volume of the Ti-substituted sample was slightly smaller than that of the unsubstituted material, in agreement with bond valence expectations [30].

To better understand the catalyst surface structure, we prepared atomistic models based on prototypical catalysts. The character of the rutile structure and transition metal vacancies can be studied with computational experiments using these models.

3.1. Energy

The difference in the total CASTEP energies for the two slabs (vacancy − no vacancy) was −156.4 eV. The CASTEP

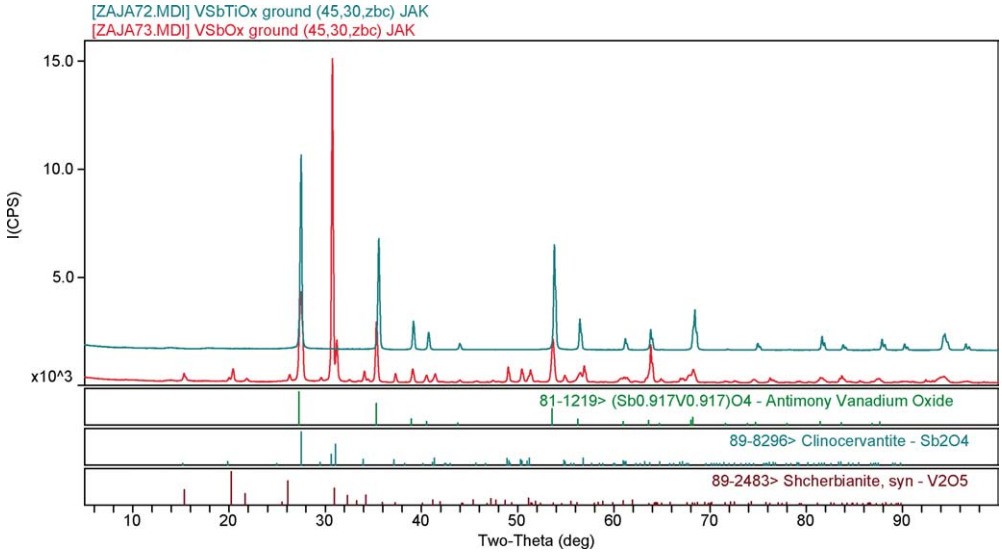

Fig. 6. X-ray powder diffraction patterns of the two ground catalysts. The top pattern is the $VSbTiO_x$ catalyst and the lower one is for $VSbO_x$.

Table 1
The phase composition and unit cell parameters for freshly prepared and ground samples determined by XRD. $VSbO_x$: $V_{0.8889}Sb_{0.8889}[\,]_{0.2222}O_4$; $VSbTiO_x$: $V_{0.7556}Sb_{0.7556}Ti_{0.30}[\,]_{0.1889}O_4$

Catalyst	$VSbO_x$	Ground $VSbO_x$	$VSbTiO_x$	Ground $VSbTiO_x$
Avg. cryst. size	Big	1400	1800	1200
Rutile $VSbO_4$ (wt%)	∼ 68	55.1(2)	100	100
a (Å)	4.628(5)	4.6209(7)	4.6187(1)	4.6173(1)
c (Å)	3.055(4)	3.0549(7)	3.0349(1)	3.0336(1)
c/a	0.660	0.661	0.657	0.657
V (Å^3)	65.44(17)	65.23(2)	64.743(3)	64.676(3)
β-Sb_2O_4 (wt%)	∼ 30	31.0(2)	–	–
V_2O_5 (wt%)	∼ 2	13.9(3)	–	–

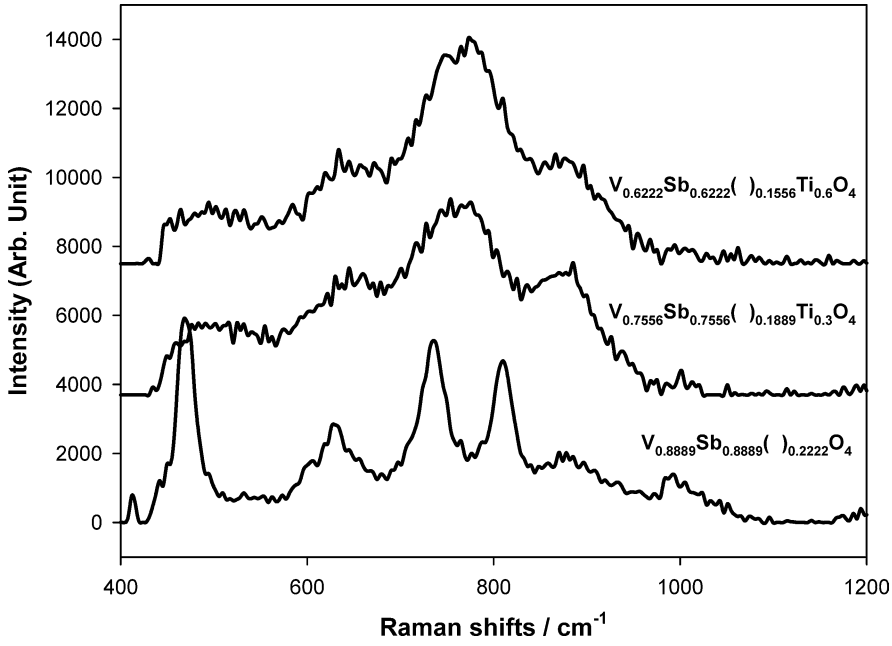

Fig. 7. UV Raman spectra of $V_{0.8889}Sb_{0.8889}[\ ]_{0.2222}O_4$, $V_{0.7556}Sb_{0.7556}[\ ]_{0.1889}Ti_{0.3}O_4$, and $V_{0.6222}Sb_{0.6222}[\ ]_{0.1556}Ti_{0.6}O_4$.

energy of an antimony atom is −150.6 eV, and so the slab with no vacancies (Fig. 1) was more stable than the slab with the 5-fold Sb defect (Fig. 2).

3.2. Structure

Fig. 3 shows a comparison of the initial (110) $VSbO_4$ (on the left) with the CASTEP optimized structure. The initial torsion angles were 180° and the initial (V,Sb)–O bond lengths were 1.98 Å above/below the surface and 2.02 Å in the surface. As the V–O–Sb–O bond is followed along the surface, the optimized structure is found to have a "kink" of approximately 15° into the surface. Furthermore, there is a slight tilting (∼ 2°) of the six-coordinate metal oxygen planes (rows of surface oxygens) toward this kink. The optimized structure also shows unique metal oxygen bond lengths. For example, vanadium has V–O bond lengths of 1.94 Å (in surface), 1.93 Å (above the surface), and 2.05 Å (below the surface). Similar results were obtained for Sb–O bonds: 1.94 Å (in the surface), 1.94 Å (above the surface), and 2.08 Å (below the surface). These results suggest that the below-surface metal–oxygen bonds are weaker than the in-surface or above-surface bonds.

The predicted vibrational spectra are in excellent agreement with experimental findings. Fig. 4 displays the experimental spectrum for the $VSbO_x$ catalyst (black) and the DMol3-predicted IR spectrum (green). In addition, for convenience, the CASTEP-optimized structure for the "pure" catalyst (i.e., no defects) is shown.

The $VSbO_x$ catalyst spectrum shows bands at 460, 630, and 745 cm^{-1} (see Figs. 7 and 8) that are attributed to bulk stretches. Vibrational analysis of these bands in the DMol3 spectrum shows that they consist of surface and subsurface

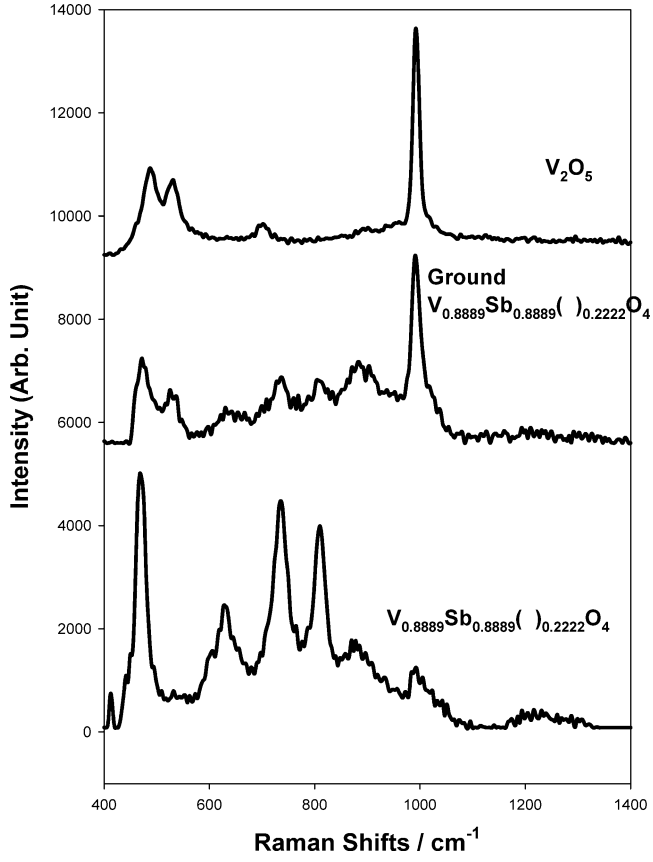

Fig. 8. UV Raman spectra of fresh and ground $V_{0.8889}Sb_{0.8889}[\ ]_{0.2222}O_4$ and V_2O_5.

bulk motions; that is, almost all of the atoms in the bulk of the slab model are moving. One general observation is that O–V–O vibrations are more prevalent between 450 and

600 cm^{-1}, whereas O–Sb–O vibrations start to dominate the motion from 600 to 750 cm^{-1}. In fact, this observation holds in general for both of the predicted spectra calculated with DMol3.

Also notice the overall agreement in the shape of the spectra (after fitting). The absence of sharp bands over 800 cm^{-1} in the predicted spectrum is another indication that these features are caused by small variations in the catalyst itself that this "pure" model cannot mimic.

Fig. 5 displays the Raman spectrum for the $VSbO_x$ catalyst (black) and the DMol3-predicted IR spectrum (red) for the CASTEP-optimized catalyst in which there is a 5-fold Sb vacancy, that is, a cation defect. Again, after the same fit as in Fig. 4, the overall agreement in the shape of the spectrum is very good. In addition, a sharp band around 858 cm^{-1} (854 and 862 cm^{-1}, respectively) appears in the predicted spectrum that had no intensity before (Fig. 4). A vibrational analysis of these peaks shows that they consist of surface symmetrical (862 cm^{-1}) and asymmetrical (854 cm^{-1}) O–Sb–O stretches adjacent to the vacancy site. The increased intensity of these peaks, compared with the experimental peak at 888 cm^{-1}, is an artifact of the model that mimics a surface with a regular Sb cation defect every other Sb atom. Obviously, the real catalyst has several different variations on this theme, which our small slab model cannot properly mimic. Our model provides good evidence that the peak around 888 cm^{-1} in the $VSbO_x$ catalyst arises from Sb vacancies at the surface.

Fig. 7 shows the UV Raman spectra of fresh $VSbO_4$ and $VSbTiO_4$ catalysts. The $VSbO_4$ catalyst exhibits bands at 468, 629, 734, 810, 880, and 990 cm^{-1}. The bands in the range of 600–810 cm^{-1}, which have not been reported previously, are prominent because of resonance enhancement at the UV excitation wavelength. Since the XRD data indicate that both V_2O_5 and β-Sb_2O_4 are present, the peaks from these phases must be considered. The peak at 990 cm^{-1} is characteristic of the V=O stretching mode of crystalline V_2O_5. The bands from β-Sb_2O_4, above 450 cm^{-1}, are located at 466, 635, and 754 cm^{-1}, with a ratio of intensities of 3:1:0.3 [31]. Fig. 7 does not show distinct peaks at 635 or 754 cm^{-1}, but their intensity may be too small to detect above the background. The peak at 468 cm^{-1} is consistent with either β-Sb_2O_4 or the rutile structure. The assignment of the peak at 880 cm^{-1} has been discussed extensively [9,13,32–34]. As shown in Section 2.1.3, this peak is typical of a cation-deficient structure and has been assigned to the M–O–M (two-coordinate oxygen) mode next to a cation vacancy. As discussed, the bands at 468, 629, 734, and 810 cm^{-1} are associated with rutile $VSbO_4$. $VSbO_4$ shows a very broad band between 700 and 900 cm^{-1} [17,20]. Deconvolution of these spectra has shown that the peak consists of two Raman bands at 835 and 795 cm^{-1} [20]. In the UV Raman spectrum, the peaks at 734 and 810 cm^{-1} are well resolved.

The Raman spectra of the Ti-substituted samples show very broad Raman peaks, and the samples with different

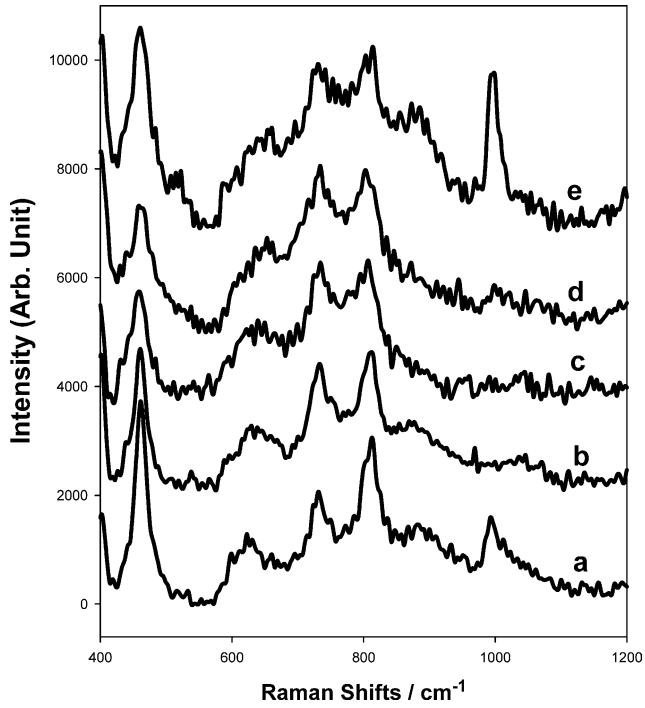

Fig. 9. UV Raman spectra of $V_{0.8889}Sb_{0.8889}[\ ]_{0.2222}O_4$ under reducing and oxidizing atmosphere: (a) fresh catalyst, (b) reduced in NH_3 for 5 min, (c) reduced in NH_3 for 10 min, (d) oxidized in air for 3 h, and (e) oxidized in air for 22 h.

Ti concentrations exhibit very similar features. The peak at 629 cm^{-1} is shifted up about 15 cm^{-1}, and the doublet at 734 and 810 cm^{-1} appears be broadened to an average peak at 753 cm^{-1} as a result of substitution. The peak at 880 cm^{-1}, which is associated with the cation vacancy site, is observed as well.

Fig. 8 shows the Raman spectra of freshly prepared and ground $VSbO_4$ catalysts together with crystalline V_2O_5. Grinding causes the relative intensities of the peaks to change dramatically. The intensities of the peaks at 468, 629, 734, and 810 cm^{-1} decrease, whereas the intensities of the bands at 880 and 990 cm^{-1} increase. A new peak at 500 cm^{-1} is assigned to crystalline V_2O_5. The peak at 468 cm^{-1} of the ground sample is a mixture of $VSbO_4$ and V_2O_5. More cation vacancy sites are formed, as shown by the increase in the relative intensity of the peak at 880 cm^{-1}. The increase in the relative intensity of the peak at 990 cm^{-1} indicates an increase in the concentration of V_2O_5. In contrast, the freshly prepared and ground samples of $VSbTiO_4$ show the same features. No new phase is formed by grinding. These results are in agreement with the XRD data.

Fig. 9 shows a sequence of Raman spectra from $VSbO_4$ after reduction in NH_3 and reoxidation in air. The peaks at 629, 734, and 810 cm^{-1} broaden after reduction and reoxidation, which suggests that the rutile structure is disordered by this treatment. The relative intensity of the peak at 468 cm^{-1} decreases after reduction and then recovers after reoxidation. This is consistent with a redox cycle of rutile structure. The peak at 990 cm^{-1} disappears completely after

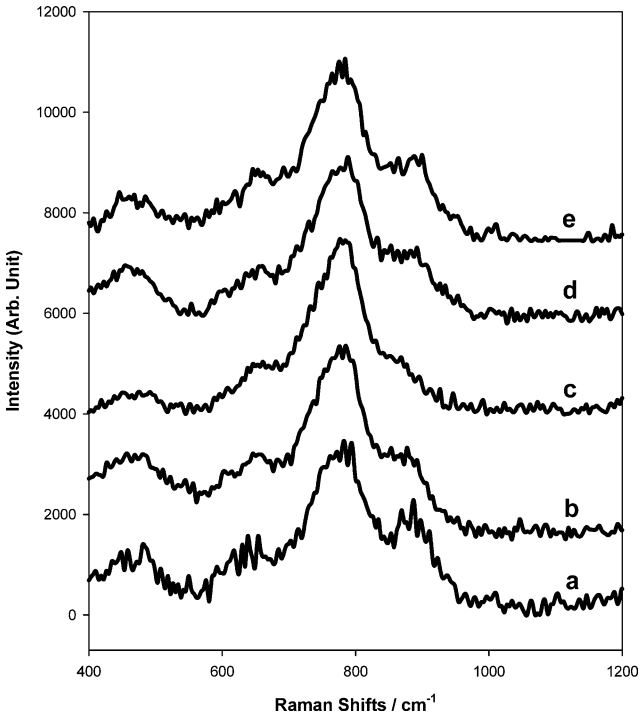

Fig. 10. UV Raman spectra of $V_{0.7556}Sb_{0.7556}[\ ]_{0.1889}Ti_{0.3}O_4$ under reducing and oxidizing atmosphere: (a) fresh catalyst, (b) reduced in NH_3 for 5 min, (c) reduced in NH_3 for 10 min, (d) oxidized in air for 3 h, and (e) oxidized in air for 22 h.

reduction for only 5 min, and then reappears only partially after reoxidation in air for 3 h. After oxidation in air for 22 h, the intensity of this peak becomes much stronger than that of the fresh sample, indicating that more V_2O_5 forms on the surface. This demonstrates that V_2O_5 is more easily reduced and reoxidized than the other components. The peak at 880 cm^{-1} is weaker after reduction for 5 min, then disappears completely after reduction for 10 min. This peak is still absent after 3 h of reoxidation, but recovers completely after 22 h under oxidizing conditions.

Fig. 10 shows the Raman spectra of $VSbTiO_4$ before and after reduction and reoxidation. The peaks at 644 and 753 cm^{-1} do not show an obvious change. The intensity of the peak at 880 cm^{-1} is gradually decreased under a reducing atmosphere and recovers after oxidation in air. It should be noted that this peak has partially recovered after reoxidation for 3 h. In comparison with $VSbO_4$, titanium-substituted $VSbO_4$ shows a more obvious change in intensity.

4. Discussion

The vanadium species are not stable in the rutile $VSbO_4$ structure. With grinding, the V–O–Sb and V–O–V bonds of rutile $VSbO_4$ break, and the vanadium species migrates to the surface to form crystalline V_2O_5. A possible explanation for this is that heat is produced during grinding and V_2O_5 is formed in the presence of O_2. This interpretation is confirmed by Raman spectra of $VSbO_4$ after a sequence of reducing and oxidizing atmospheres. The V_2O_5 phase disappears after being reduced in NH_3, but additional crystalline V_2O_5 is formed after reoxidation in air. V_2O_5 has been reported to convert to V_4O_9 after catalytic testing [9]. We find no evidence for the formation of new crystalline phases. On the contrary, the vanadium species in Ti-substituted $VSbO_4$ are very stable. There is no V_2O_5 phase detectable on a freshly prepared sample. After grinding and oxidizing in air, no new phase was detected. This indicates that substituted titanium helps to stabilize vanadium in the rutile structure, totally avoiding the formation of surface V_2O_5. In the literature, Fe substitution in $VSbO_4$ has a similar effect in the stabilization of antimony [16]. After catalytic reaction the surface antimony content remains constant for $FeVSbO_4$, whereas the concentration of SbO_x is increased for $VSbO_4$. The explanation is that Sb^{5+} in the rutile structure is reduced to Sb^{3+} under a reducing reaction atmosphere. Sb^{3+} is not stable in the rutile structure and tends to form SbO_x on the surface. Fe substitution may lead to a less selective catalyst, since SbO_x is selective for the formation of acrylonitrile [9]. In the rutile $VSbO_4$ structure the valence state of V is 3+ or 4+ [32]. V^{5+} is not stable in the rutile structure and tends to form V_2O_5 on the surface under an oxidizing atmosphere [35]. Ti^{4+} plays a role in limiting the oxidation of V^{3+} and V^{4+} in the rutile structure, hence preventing the formation of crystalline V_2O_5. Andersson points out that free vanadia promotes the conversion of ammonia to nitrogen, and V–O–V moieties are active for degradation and combustion [2,33]. Therefore, replacement of V with Ti has a positive influence on the selectivity by preventing the formation of free vanadia. This interpretation does not invoke "site isolation" of vanadia, a concept that has been invoked previously to explain the effect of titania [15].

After grinding, the concentration of β-Sb_2O_4 is constant but the concentration of V_2O_5 increases significantly. One question that remains is whether the formation of V_2O_5 leads to a change in the composition of the rutile structure. The unit cell parameters have been shown to be sensitive to the composition of the rutile structure [32]. With an increase in the ratio $n(V)/n(Sb)$, the cell parameter a increases, but c decreases. However, in Table 1 no significant changes in the cell parameters are observed. That means that the composition of the rutile structure does not change dramatically. The Raman spectra in Fig. 8 support this conclusion. Since no new β-Sb_2O_4 is formed on the surface, the extra antimony moieties may form amorphous SbO_x on the surface. The absence of crystalline SbO_x is reasonable because the formation of α- and β-Sb_2O_4 phases requires higher temperatures [31].

The role of the cation vacancy sites in propane ammoxidation has been studied extensively [12,14,16]. The Raman peak associated with the cation vacancy sites nearly disappears after the reaction, which implies that the two-coordinate oxygen associated with the cation vacancy sites reacts readily with ammonia. Roussel [16] pointed out that the catalytic activity is related to the presence of defects.

More defect sites result in higher activity. In addition, selectivity is also correlated with the concentration of cation vacancies. The selectivity for propylene increases with the increasing number of defect sites [16]. Oxygen in the rutile structure is usually three-coordinate, but the two-coordinate oxygen species is formed when cation vacancies are created in the structure. In the Raman spectra, the peak at 880 cm^{-1} has been assigned to the two-coordinate oxygen next to the defect site, whereas in the IR spectra two peaks at 880 and 1016 cm^{-1} are associated with cation vacancies. The relative intensity of the peak at 880 cm^{-1} is proportional to the concentration of the cation vacancies [32]. It was suggested that the possibility of two-coordinate oxygen is in the following sequence: Sb–O–Sb > Sb–O–V > V–O–V [33]. The peak at 880 cm^{-1} is assigned to Sb–O–Sb, and the band at 1016 cm^{-1} is associated with Sb–O–V [9]. In this study the Raman peak at 880 cm^{-1} is found to be sensitive to NH_3 and air. The intensity of the peak decreases with the presence of NH_3 and increases in air to complete a redox cycle. The other peaks at 629, 734, and 810 cm^{-1} broaden but do not disappear. This indicates that NH_3 is apt to react with Sb–O–Sb next to cation vacancies. It has been established that antimony moieties are active for the formation of acrylonitrile, and a bridging Sb–NH–Sb species is responsible for the nitrogen insertion [36]. The activation of ammonia over antimonite catalysts is proposed to proceed as follows:

$$\text{Sb–O–Sb} + \text{NH}_3 \rightarrow \text{Sb–NH–Sb} + \text{H}_2\text{O},$$

$$\text{C}_3\text{H}_8 + [\,]\text{–V–O} + \text{Sb–O–V} \rightarrow \text{C}_3\text{H}_6 + [\,]\text{–V–OH} + \text{Sb–OH–V},$$

$$\text{Sb–NH–Sb} + \text{C}_3\text{H}_6 + \text{O}_2 \rightarrow \text{Sb–O–Sb} + \text{C}_3\text{H}_3\text{N} + 2\text{H}_2\text{O},$$

where [ ]–V–O corresponds to V adjacent to a cation vacancy, [ ].

It was suggested that the defect site leads to the formation of a more active oxygen atom, which is responsible for the hydrogen abstraction that forms propylene [14]. The formation of Sb–NH–Sb next to the defect site is advantageous for the N insertion step because of to a steric effect. Compared with $VSbO_4$, the Ti-substituted sample shows a more obvious change in intensity of the two-coordinate oxygen peak. In the literature, TPR results show that Ti substitution changes the oxidation–reduction properties of the rutile phase [37]. The first TPR peak is shifted to a lower temperature, and the second one appears at a higher temperature. It was suggested that this leads to a more efficient redox system and improves the selectivity. Our result is consistent with the TPR data and indicates that the substitution of titanium facilitates the reduction and oxidation of the catalysts and improves their overall catalytic properties.

5. Conclusions

1. UV Raman spectra of $VSbO_4$ and $VSbTiO_4$ catalysts show peaks at 468, 600–800, 880, and 990 cm^{-1}. These bands are assigned to the bulk rutile, two-coordinated oxygen next to a cation vacancy, and V_2O_5, respectively.
2. Titanium stabilizes the V^{3+} or V^{4+} in the rutile structure, preventing the formation of the V_2O_5 on the surface by grinding.
3. UV Raman spectroscopy was used to study the active sites in $VSbO_4$ and $VSbTiO_4$ catalysts in oxidizing and reducing atmospheres. The peak associated with cation vacancy sites decreases in intensity after reduction and then recovers after oxidation. The two-coordinate oxygen peak on the Ti-substituted sample shows a more obvious change, which indicates that the addition of titanium improves the reduction and oxidation ability of the catalysts.

Acknowledgment

G.X. and P.C.S. gratefully acknowledge financial support from BP Chemicals for this project.

References

[1] J.D. Idol, US Patent 2 904 580 (1959).
[2] A.T. Guttmann, R.K. Grasselli, J.F. Brazdil, US Patent 4 746 641 (1988).
[3] J.F. Brazdil, M.A. Toft, L.C. Glaeser, US Patent 5 008 427 (1991).
[4] G. Centi, S. Perathoner, F. Trifirò, Appl. Catal. 157 (1997) 143.
[5] G. Centi, R.K. Grasselli, E. Patanè, F. Trifirò, Stud. Surf. Sci. Catal. 55 (1990) 515.
[6] R.K. Grasselli, G. Centi, F. Trifirò, Appl. Catal. 57 (1990) 149.
[7] G. Centi, R.K. Grasselli, F. Trifirò, Catal. Today 13 (1992) 661.
[8] R. Nilsson, T. Lindblad, A. Andersson, C. Song, S. Hansen, Stud. Surf. Sci. Catal. 82 (1994) 293.
[9] R. Nilsson, T. Lindblad, A. Andersson, J. Catal. 148 (1994) 501.
[10] G. Centi, S. Perathoner, Appl. Catal. A 124 (1995) 317.
[11] J. Nilsson, A.R. Landa-Cánovas, S. Hansen, A. Andersson, J. Catal. 160 (1996) 244.
[12] J. Nilsson, A.R. Landa-Cánovas, S. Hansen, A. Andersson, J. Catal. 186 (1999) 442.
[13] A. Wickman, L.R. Wallenberg, A. Andersson, J. Catal. 194 (2000) 153.
[14] T. Shishido, T. Konishi, I. Matsuura, Y. Wang, K. Takaki, K. Takehira, Catal. Today 71 (2001) 77.
[15] A. Andersson, S. Hansen, A. Wickman, Top. Catal. 15 (2001) 103.
[16] H. Roussel, B. Mehlomakulu, F. Belhadj, E. van Steen, J.M.M. Miller, J. Catal. 205 (2002) 97.
[17] M.O. Guerrero-Pérez, J.L.G. Fierro, M.A. Vicente, M.A. Bañares, J. Catal. 206 (2002) 339.
[18] A. Mimura, K. Ohyachi, I. Matsuura, Sci. Tech. Catal. (1998) 69.
[19] C.L. Pieck, M.A. Bañares, M.A. Vicente, J.L.G. Fierro, Chem. Mater. 13 (2001) 1174.
[20] M.O. Guerrero-Pérez, M.A. Bañares, Chem. Commun. (2002) 1292.
[21] T. Shishido, A. Inoue, T. Konishi, I. Matsuura, K. Takehira, Catal. Lett. 68 (2000) 215.
[22] Y.T. Chua, P. Stair, J. Catal. 196 (2000) 66.
[23] P.C. Stair, J. Vac. Sci. Technol. A 15 (1997) 1679.
[24] G. Xiong, Z.C. Feng, J. Li, Q.H. Yang, P.L. Ying, Q. Xin, C. Li, J. Phys. Chem. B 104 (2000) 3581.
[25] C. Li, J. Catal. 216 (2003) 203.
[26] For more detail, please see www.accelrys.com.

[27] M.C. Payne, E. Tarnow, P.D. Bristowe, J.D. Joannopoulos, Mol. Simul. 4 (1989) 79.
[28] Materials Studio DMol3 v3.0 Copyright 2003, Accelrys Inc. All rights reserved;
B. Delley, J. Chem. Phys. 92 (1990) 508;
B. Delley, J. Chem. Phys. 113 (2000) 7756.
[29] A.C. Larson, R.B. Von Dreele, General Structure Analysis System (GSAS), Los Alamos National Laboratory, Report LAUR 86-748 (2000).
[30] N.E. Breese, M. O'Keefe, Acta Crystallogr. B 47 (1991) 192–197.
[31] C.A. Cody, L. Dicarlo, R.K. Darlington, Inorg. Chem. 6 (1979) 1572.
[32] A. Landa-Cánovas, J. Nilsson, S. Hansen, K. Ståhl, A. Andersson, J. Solid State Chem. 116 (1995) 369.
[33] A. Andersson, S.L.T. Andersson, G. Centi, R.K. Grasselli, M. Sanati, F. Trifirò, Appl. Catal. A 113 (1994) 43.
[34] S. Hansen, K. Ståhl, R. Nilsson, A. Andersson, J. Solid State Chem. 102 (1993) 340.
[35] H.W. Zanthoff, W. Crünert, S. Buchholz, M. Heber, L. Stievano, F.E. Wagner, G.U. Wolf, J. Mol. Catal. A 162 (2000) 435.
[36] J.D. Burrington, C.T. Kartisek, R.K. Grasselli, J. Catal. 87 (1984) 363.
[37] A. Barbaro, S. Larrondo, S. Duhalde, N. Amadeo, Appl. Catal. A 193 (2000) 277.